

Article

# Sequence Control Strategy for Grid-Forming Voltage Source Converters Based on the Virtual-Flux Orientation under Balanced and Unbalanced Faults

Juan Dolado Fernández <sup>1</sup>, Joaquín Eloy-García <sup>2</sup>, Santiago Arnaltes <sup>1,\*</sup> and Jose Luis Rodríguez-Amenedo <sup>1</sup>

<sup>1</sup> Electrical Engineering Department, Superior Polytechnique School, Faculty of Engineering, Carlos III University of Madrid, 28911 Leganés, Madrid, Spain

<sup>2</sup> Ingenia Power Solutions SL, Av. Transición Española 32, 28918 Alcobendas, Madrid, Spain

\* Correspondence: arnalte@ing.uc3m.es

**Abstract:** Renewable power generation has increased in recent years, which has led to a decrease in the use of synchronous generators (SGs). These power plants are mainly connected to the power system through electronic converters. One of the main differences between electronic converters connected to power systems and SGs connected to the grid is the current contribution during faults, which can have an impact on protection systems. New grid codes set requirements for fast current injection, but the converters' maximum current limitation during faults make it challenging to develop control strategies for such current contribution. This paper presents a positive and negative sequence current injection strategy according to the new Spanish grid code requirements for the novel grid-forming converter control algorithm based on virtual-flux orientation. The behavior of the proposed strategy is tested in a hardware in the loop (HiL) experimental set-up under balanced faults, meaning that the fault is symmetrically distributed among the three phases, and unbalanced faults, where the fault current is distributed asymmetrically between the phases.

**Keywords:** grid-forming power converter; virtual-flux orientation; unbalanced faults; negative sequence; hardware in the loop; renewable energy sources; Spanish grid code

**Citation:** Dolado Fernández, J.; Eloy-García, J.; Arnaltes, S.; Rodríguez-Amenedo, J.L. Sequence Control Strategy for Grid-Forming Voltage Source Converters Based on the Virtual-Flux Orientation under Balanced and Unbalanced Faults. *Energies* **2023**, *16*, 3056. <https://doi.org/10.3390/en16073056>

Academic Editor: Ahmed Abu-Siada

Received: 22 February 2023

Revised: 22 March 2023

Accepted: 24 March 2023

Published: 27 March 2023



**Copyright:** © 2023 by the authors. Licensee MDPI, Basel, Switzerland. This article is an open access article distributed under the terms and conditions of the Creative Commons Attribution (CC BY) license (<https://creativecommons.org/licenses/by/4.0/>).

## 1. Introduction

The power generation landscape is widely recognized to have undergone a significant transformation as a result of the extensive integration of renewable energy sources (RES) into power systems around the world. The integration of RES into power systems has significantly transformed the electrical generation model, with more renewable power capacity added to the grid annually than all fossil fuels and nuclear power combined.

According to recent studies [1], some electricity systems are experiencing scenarios of close to 100% hourly penetration of RES into the grid. This trend, as reported by the International Renewable Energy Agency (IRENA) [2], shows that power systems are increasingly dominated by renewable power plants that use inverter-based resources (IBRs) for grid connection rather than conventional SGs.

A decentralized power system, characterized by the integration of RES at the distribution level, is replacing the traditional centralized system that relied on large SG for stability and robustness. Within this new generation model, IBRs can be grouped into two categories: grid-forming (GFM) converters and grid-following (GFL) converters, which are the most commonly used type in grid-connected systems.

GFMs are based on maintaining the internal voltage phasor angle and modulus during the subtransient and transient periods, replicating the same behavior as an SG [3].

Inertial response and damping of power oscillations can be provided by GFMs [4], which are also capable of operating in islanded mode and low-system-strength conditions.

On the other hand, GFL relies on a phase-locked loop (PLL) to synchronize their internal voltage and current signals with the grid voltage, as well as a fast-current controller to regulate the active and reactive power injected into the grid. However, the control structure of GFLs can become unstable under certain low-inertia systems [5,6]. Additionally, GFL converters may not be able to provide inertial response and do not support islanded operation, meaning they may not be able to help restoring power in case of a blackout [7]. Consequently, GFMs have arisen as a powerful alternative to overcome the limitations of GFLs.

Three main categories of GFM controllers have been proposed in the literature, classified according to their operating principles [8]. These include droop controls, which allow parallel operation of several converters, simulating the governor action of synchronous generators [9–11]. Another category is synchronous machine-based control, which incorporates the inertia and damping properties of synchronous generators [12–15]. Finally, nonlinear methods, such as the virtual oscillation-based method [16–18], are also included in this category.

The ability to limit current in GFMs is a crucial aspect to consider in their design. During events such as voltage dips or major grid disturbances, the current may exceed the converter's nominal value, and the power electronics, unlike the SGs, can only withstand small over currents (usually in the range of 1.1–1.3 p.u.) [19,20]. Various strategies have been proposed in the literature to address this issue, such as adding current-limiting blocks between voltage and current control loops [21–23], switching to a GFL control mode during faults [24], or utilizing virtual impedances [25–27].

In addition, the integration of renewable energy sources into power systems has resulted in the need for these generators to help maintaining voltage during faults in the electric power system, as outlined in grid codes [28–30].

Some grid codes only require positive sequence current injection under balanced and unbalanced faults [31], but this can provoke an overvoltage in healthy phases during asymmetrical faults and negatively impact the safety of the system [32]. Furthermore, the absence of negative sequence current injection can also have a detrimental impact on the performance of protective systems, as several functions of the protection relays depend on negative sequence magnitudes, which signify imbalanced system conditions [33–35].

The latest grid regulations, such as Greece or Germany, have established the requirement for both positive and negative sequence current injections in order to overcome drawbacks [36,37]. Another example of this can be seen in the Spanish transmission system operator (Red Eléctrica de España, REE) Operating Procedure 12.2 [38], which describes the requirements for positive and negative sequence current injection during faults.

Due to the requirements established by the newest grid codes, negative sequence current injection strategies during unbalanced faults have been extensively covered by the literature for GFL converters [39–42]. However, this has not yet been achieved with GFM converters. Considering their importance as an alternative to overcome the limitations of GFL converters in terms of instability, inertial response, and islanding capability, effective methodologies must be developed to comply with the guidelines established by the new grid codes. A recent publication [43] has introduced a novel control scheme for GFMs. This scheme presents an innovative solution that regulates a state variable, referred to as virtual flux, calculated as a function of the output current and the integral of the voltage measured at the converter's terminals. Furthermore, the publication proposes a new method for limiting both active and reactive current, which does not rely on internal current control loops.

The main objective of this paper is to propose for this novel type of grid-forming converters a balanced and unbalanced faults control strategy based on REE Operating

Procedure 12.2, which states that the amount of positive and negative sequence reactive current injected during the fault must be proportional to the depth of the voltage dip.

To achieve this purpose, first, a sequence extraction algorithm has been added to the original model. In addition, the ACC+ and RCC+ blocks for control of the positive sequence active and reactive currents during the faults have been developed in a novel way, directly affecting the control angle and the reference virtual flux modulus, respectively, as will be seen below.

On the other hand, ACC- and RCC- blocks have been designed to provide the necessary negative sequence active and reactive currents during the faults. Lastly, the calculation of the voltage setpoints through the reference voltages of each sequence has also been included.

This article is organized as follows. Section 2 provides a description of the voltage source converter (VSC) system. Section 3 summarizes the requirements of the Spanish grid code for balanced and unbalanced faults. The control system for GFM based on the virtual-flux orientation and a novel strategy for handling balanced and unbalanced faults is introduced in Section 4. Section 5 presents the results obtained and a comparison with the original control strategy. The final section presents the conclusions.

## 2. System Description

This section presents the components of a GFM converter connected to the grid. The single line diagram shown in Figure 1 illustrates a grid modeled as a three-phase voltage source of constant frequency and an internal impedance. The VSC is connected to the grid through an LCL filter with parameters  $R_f$ ,  $L_f$ , and  $C_f$ , which includes a step-up transformer. The constant voltage source at the DC bus terminals is  $V_{dc}$  and the input current is  $I_{dc}$ .

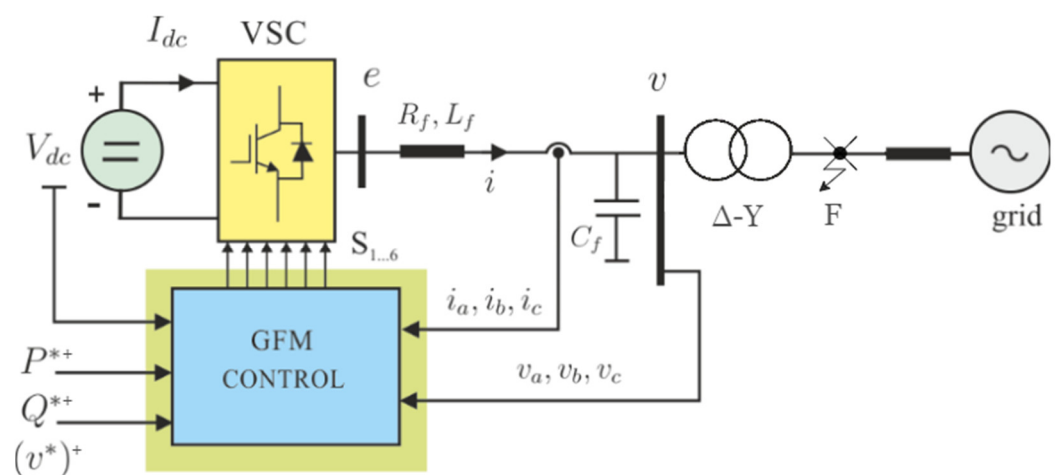


**Figure 1.** System description of a GFM connected to a grid.

The GFM is controlled by measuring the three-phase voltage  $v_a, v_b, v_c$ , and currents  $i_a, i_b, i_c$  at the AC side. To generate the switching pattern  $S_{1...6}$ , which determines the state of the switches of the converter, the voltage measure  $V_{dc}$  is also required. Furthermore, the GFM can be controlled as a PQ node by setting the positive sequence active  $P^{*+}$  and reactive  $Q^{*+}$  power setpoints. Alternatively, the converter can be controlled as a PV node by setting a voltage reference  $v^{*+}$  instead of a reactive power setpoint. Finally, Figure 1 shows point F, where the balanced and unbalanced faults of the tests performed are provoked.

### 3. Spanish Grid Code Requirements under Balanced and Unbalanced Faults Review

According to [38], generating modules are classified into four types depending on its maximum capacity and/or the voltage at the connection point (PCC): Type A, Type B, Type C, and Type D. Table 1 shows this classification.

**Table 1.** Power generating module types according to the Spanish grid code [38].

Power Generating Module Type	Voltage at the Connection Point	Maximum Capacity
Type A	$V_{PCC} < 110 \text{ kV}$	$0.8 \text{ kW} \leq P_{max} < 110 \text{ kW}$
Type B	$V_{PCC} < 110 \text{ kV}$	$100 \text{ kW} \leq P_{max} < 5 \text{ MW}$
Type C	$V_{PCC} < 110 \text{ kV}$	$5 \text{ MW} \leq P_{max} < 50 \text{ MW}$
Type D	$V_{PCC} \geq 110 \text{ kV}$	$P_{max} \geq 50 \text{ MW}$

Type A generating modules are not considered in this paper because it is not a requirement for them to provide low-voltage ride-through (LVRT) control. In addition, as this paper is focused on generating modules that are connected to a medium-voltage distribution grid, Type D generating modules are excluded because these modules operate at voltages above 110 kV. Therefore, only Type B and Type C have been considered for the tests performed in this document.

The Spanish grid code published in July 2020 describes the current injection requirements for Type B and Type C modules during balanced and unbalanced faults. Figure 2 shows the positive sequence and negative sequence reactive current injection/absorption to be provided by the converter during faults.

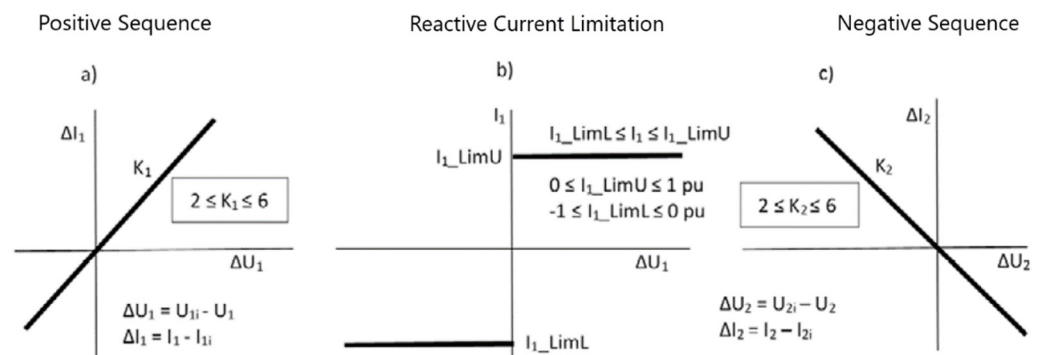


**Figure 2.** (a) Positive sequence reactive current injection/absorption additionally required proportional to the positive sequence voltage error; (b) positive sequence total reactive current injection/absorption limitation; (c) negative sequence reactive current injection/absorption additionally required proportional to the negative sequence voltage error [38].

When the fault is balanced, the module must inject or absorb a certain positive sequence reactive current additional to the existing reactive current before the fault,  $\Delta I_1$  (p.u.), proportionally to the positive sequence voltage error,  $\Delta U_1$  (p.u.). The value of the  $K_1$  constant is adjustable between 2 and 6, 3.5 being its usual value. Additionally to the total reactive current, the module must inject active current until reaching the value of the rated current.

On the other hand, when the fault is unbalanced, the module must inject or absorb the positive sequence reactive current  $\Delta I_1$  and a certain negative sequence reactive current,  $\Delta I_2$  (p.u.), proportionally to the negative sequence voltage error,  $\Delta U_2$  (p.u.). The value of the  $K_2$  constant is also adjustable between 2 and 6, 3.5 being its usual value. In the same way as for balanced faults, the converter must additionally inject positive sequence active current until the rated current value is reached.

Finally, Figure 2b shows the limit for the total reactive current, where the default values are  $I_{r\_limU} = 0.9$  p.u. and  $I_{r\_limU} = -0.9$  p.u, allowing a maximum value of 1 p.u.

#### 4. Sequence Control Strategy

This section presents the control strategy proposed to comply with the Spanish grid code during unbalanced faults. First, the sequences extraction algorithm is explained. Next, the positive sequence control is summarized, which is quite similar to the one proposed in [43] but with some slight modifications to control the amount of active and reactive current setpoints during the fault.

Then, a detailed scheme of the proposed control for the negative sequence components, which only acts during the fault, is presented. Finally, once the converter voltage references of both sequences  $e_d^+$ ,  $e_q^+$ ,  $e_d^-$  and  $e_q^-$  are obtained, the switching pattern  $S_{1...6}$  can be generated.

##### 4.1. Sequences Extraction Algorithm

In order to obtain the positive and negative sequences' voltage and current components, the algorithm illustrated in Figure 3 has been employed. Both sequences, as shown in Figure 3, are obtained from the  $\alpha\beta$  components and the components delayed one quarter of the period.

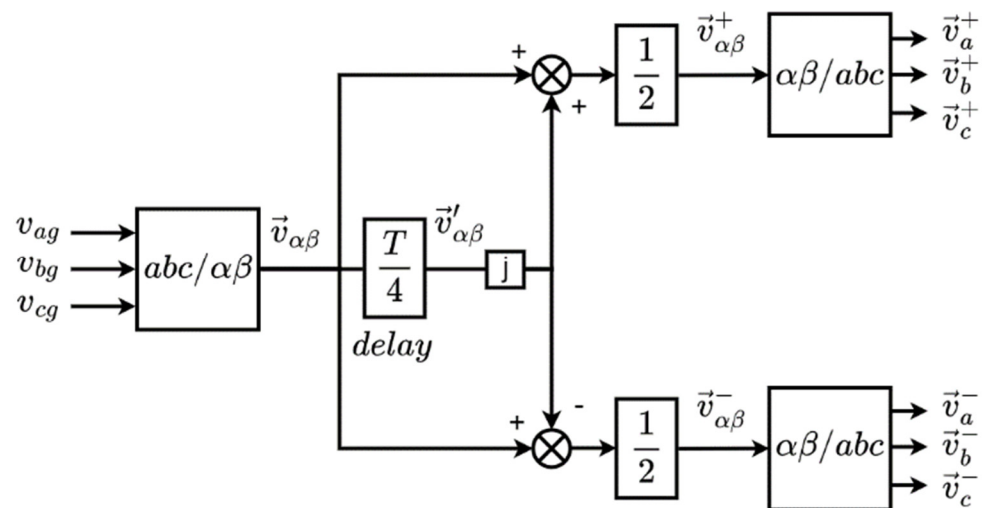


Figure 3. Sequence extraction algorithm.

Thus, the positive sequence voltages are obtained as:

$$v_{\alpha}^{+} = \frac{1}{2}(v_{\alpha} - v'_{\beta}) \quad (1)$$

$$v_{\beta}^{+} = \frac{1}{2}(v_{\beta} + v'_{\alpha}) \quad (2)$$

and the negative sequence components yield:

$$v_{\alpha}^{-} = \frac{1}{2}(v_{\alpha} + v'_{\beta}) \quad (3)$$

$$v_{\beta}^{-} = \frac{1}{2}(v_{\beta} - v'_{\alpha}) \quad (4)$$

where  $v_{\alpha}$  and  $v_{\beta}$  are the  $\alpha\beta$  components and  $v'_{\alpha}$  and  $v'_{\beta}$  are these components delayed. The same process is applied to extract the current sequence components.

4.2. Positive Sequence Control Scheme

The proposed GFM control scheme for the positive sequence is shown in Figure 4, which is composed of four blocks. The virtual-flux measurement (VFM) block calculates the positive sequence variable state for each phase,  $\psi_{kv}^+$ , by integrating the positive sequence voltage,  $v_k^+$ , plus the product of the positive sequence current,  $i_k^+$ , and the filter inductance. The calculation is expressed as follows, where  $k=a,b,c$  denotes the phase:

$$\psi_{kv}^+ = L_f i_k^+ + \int v_k^+ dt \tag{5}$$

Afterwards, a Clarke transformation is applied to obtain the  $\alpha\beta$  components of the positive sequence virtual flux, yielding:

$$\psi_{\alpha v}^+ = L_f i_{\alpha}^+ + \int v_{\alpha}^+ dt \tag{6}$$

$$\psi_{\beta v}^+ = L_f i_{\beta}^+ + \int v_{\beta}^+ dt \tag{7}$$

In addition, within this block, the value of the positive active power  $P^+$  and positive reactive power  $Q^+$  are obtained as follows:

$$P^+ = \frac{3}{2}(v_{\alpha}^+ i_{\alpha}^+ + v_{\beta}^+ i_{\beta}^+) \tag{8}$$

$$Q^+ = \frac{3}{2}(v_{\beta}^+ i_{\alpha}^+ - v_{\alpha}^+ i_{\beta}^+) \tag{9}$$

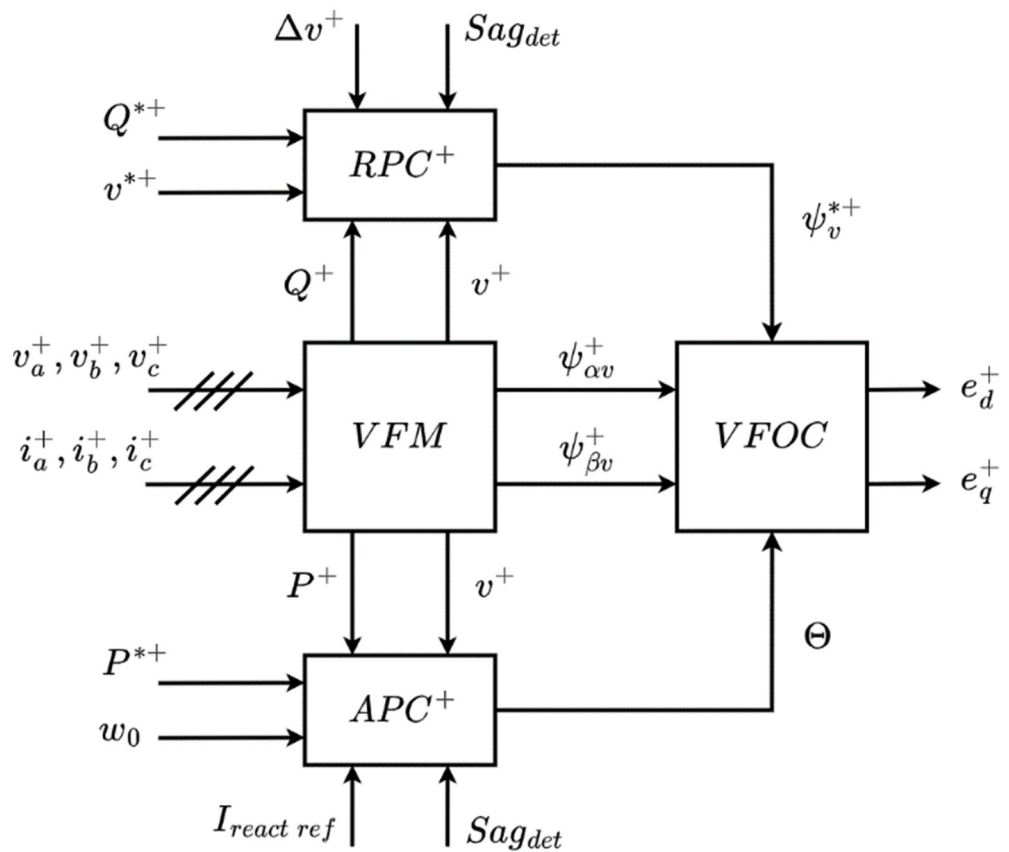


Figure 4. Positive sequence control scheme.

The positive active power controller ( $APC^+$ ) block depicted in Figure 4 is shown in Figure 5. This block calculates the control angle  $\theta$  along which the positive sequence virtual-flux vector  $\vec{\psi}_v^+$  must be oriented to reproduce the SG's swing equation. The internal frequency  $\omega'^+$  is obtained from the equation:

$$P^{*+} - P^+ = T_m \frac{d\omega'^+}{dt} + D(\omega'^+ - \omega_0) \tag{10}$$

where the reference active power is represented by  $P^{*+}$ , the measurement of the active power is denoted by  $P^+$ , and the inertia is represented by  $T_m$ , given in seconds and defined as twice the inertia constant  $H$  ( $T_m = 2H$ ). The damping factor, in per unit, is denoted by  $D$  and  $\omega_0$  represents the rated frequency in rad/s.

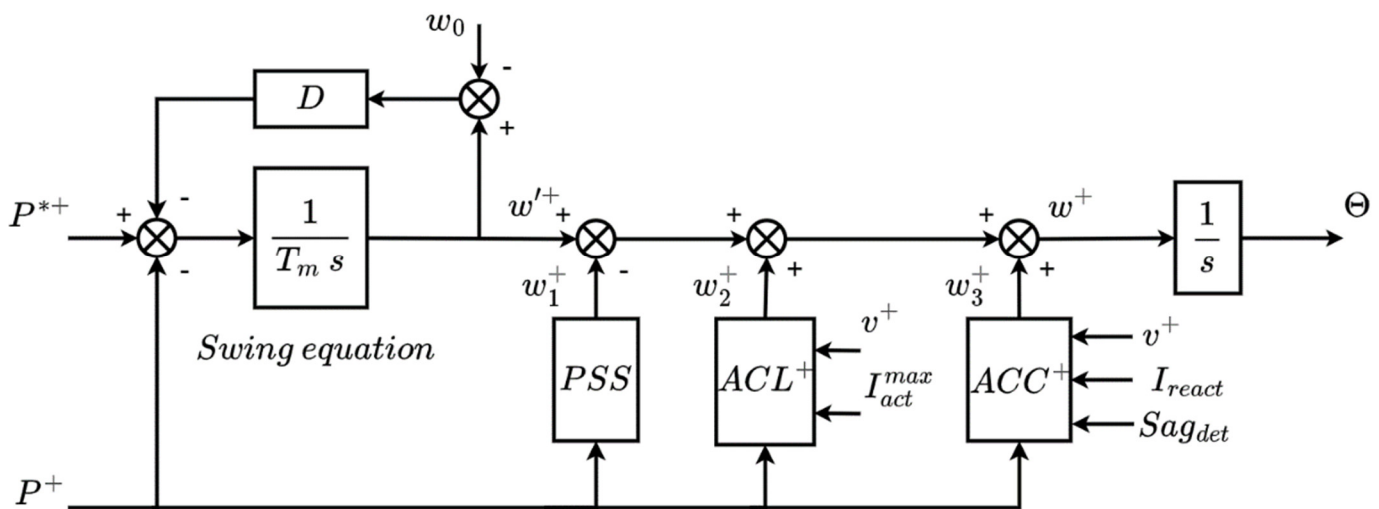


Figure 5. Positive active power controller block.

As is depicted in Figure 5, the angle  $\theta$  is obtained by the integration of the frequency  $\omega^+$ , which can also be expressed as the internal frequency  $\omega'^+$  minus  $\omega_1^+$  plus  $\omega_2^+$  and  $\omega_3^+$ , yielding:

$$\theta = \int \omega^+ dt = \int [\omega'^+ - \omega_1^+ + \omega_2^+ + \omega_3^+] dt \tag{11}$$

where  $\omega'^+$  is the internal frequency obtained from the swing equation.  $\omega_1^+$  is the output of the power system stabilizer (PSS) block, which is added in order to compensate the insufficiently damped active power response when the inertia constant is significant and the damping factor is low.  $\omega_2^+$  is the output of the positive active current limiting ( $ACL^+$ ) block, which ensures that the maximum active current value,  $I_{act}^{max}$ , is not exceeded. When this limit is approached, the  $ACL^+$  block restricts the control angle  $\theta$ , thereby limiting the active current module [43].

As a new feature in this control loop, the positive active current controller ( $ACC^+$ ) block shown in Figure 6 has been added, which only acts when a voltage fault is detected ( $Sag_{det}$  signal equals to 1). The output of this block is the frequency  $\omega_3^+$ .

As stated in the Spanish grid code, in the event of a fault, in addition to the reactive current injected, the converter must inject positive sequence active current up to the value of the rated current of the converter if there is remaining current headroom. This will depend on fault type, voltage depth, and constant K setting. More details will be provided below. To ensure that the maximum value of the current provided by the converter is reached and not exceeded, it must be ensured that:

$$I_{mod}^+ + I_{mod}^- = 1 \tag{12}$$

where  $I_{mod}^+$  and  $I_{mod}^-$  are the positive and negative current modulus, respectively. As during the faults and only in case of unbalanced, the negative sequence current that will exist will be the  $I_{react}^-$ , and (11) can be expressed as:

$$I_{mod}^+ + I_{react}^- = 1 \tag{13}$$

where  $I_{mod}^+$  is defined as:

$$I_{mod}^+ = \sqrt{(I_{act}^+)^2 + (I_{react}^+)^2} \tag{14}$$

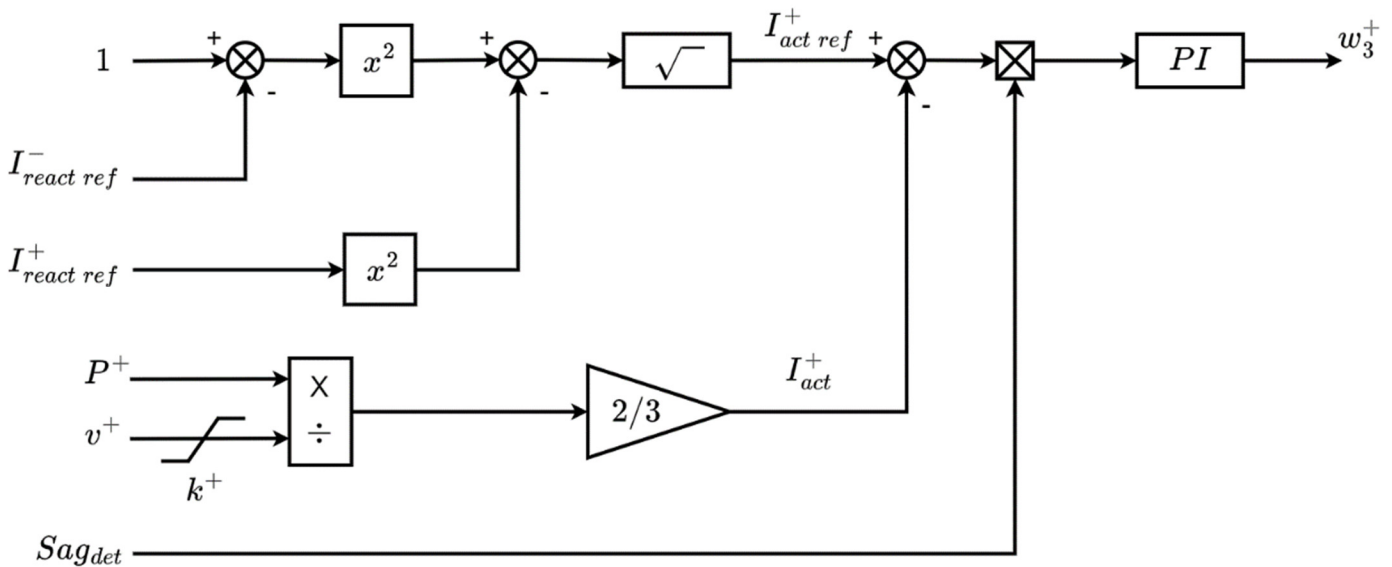


Figure 6. Positive active current controller block.

Therefore, replacing (13) in (12) and using the value of the current references instead of their instantaneous value yields:

$$\sqrt{(I_{act ref}^+)^2 + (I_{react ref}^+)^2} + I_{react ref}^- = 1 \tag{15}$$

By subtracting from the equation,  $I_{act ref}^+$  is obtained:

$$I_{act ref}^+ = \sqrt{(1 - I_{react ref}^-)^2 - (I_{react ref}^+)^2} \tag{16}$$

When a voltage dip is detected ( $Sag_{det}$  signal equals to 1), the error between  $I_{act ref}^+$  and the positive sequence active current module  $I_{act}^+$  is passed through a proportional-integral (PI) regulator to obtain  $\omega_3^+$ , which modifies the angle  $\theta$  until the  $I_{act ref}^+$  is reached. The  $I_{act}^+$  current is calculated from:

$$P^+ = \frac{3}{2} v^+ I_{act}^+ \tag{17}$$

where the positive sequence module of the voltage  $v^+$  is limited to a value greater than zero ( $k^+$ ) to avoid indeterminacies.

The positive reactive power controller ( $RPC^+$ ) block depicted in Figure 4 is illustrated in Figure 7. The inputs of this block, depending on whether the VSC is operating as a PQ node or a PV node, are the positive sequence reference and measured reactive power ( $Q^{+*}$  and  $Q^+$ , respectively) or voltage ( $v^{+*}$  and  $v^+$ ). As indicated in [43], the reactive

power exchanged by the converter depends on the difference between the module of the internal voltage  $e$  and the grid voltage  $v$ , where  $e$  is proportional to  $\psi_v^*$ . So, the reactive power can be controlled by a droop control where the virtual-flux module reference is obtained as:

$$\psi_v^* = \psi_{v0} + n_q(Q - Q^*) \tag{18}$$

$\psi_{v0}$  being an initial virtual flux set to 1 p.u. and  $n_q$  the droop gain. In this case, the positive sequence modulus of the reference virtual flux is calculated using the positive sequence components of  $v$  and  $Q$ . Furthermore, there are two additional terms in the proposed control loop,  $\Delta\psi_{v1}^{*+}$  and  $\Delta\psi_{v2}^{*+}$ .

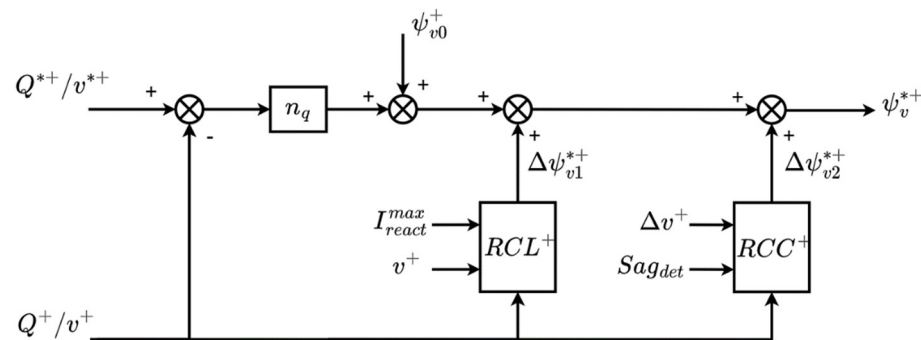


Figure 7. Positive reactive power controller block.

The first one is the positive reactive current limiting ( $RCL^+$ ) block output,  $\Delta\psi_{v1}^{*+}$ , which, similarly to the  $ACL^+$  block, ensures that the maximum positive sequence reactive current value,  $I_{react}^{max}$ , is not exceeded. When this limit is approached, the  $RCL^+$  block reduces the virtual-flux module reference, limiting as well the reactive current [43].

The second term is the output of the positive reactive current controller ( $RCC^+$ ) block,  $\Delta\psi_{v2}^{*+}$ , being the novelty within this control loop. This block is shown in Figure 8 and operates in a very similar way as the  $ACC^+$  loop. According to the Spanish grid code, when a fault occurs, the VSC must inject positive sequence reactive current additional to the pre-fault reactive current and proportional to the positive sequence voltage error ( $\Delta v^+$ ). As the pre-fault positive sequence reactive current is very low before the fault, this is disregarded for the tests performed, assuming that  $I_{react\ ref}^+$  is equal to  $\Delta I_{react}^+$ .

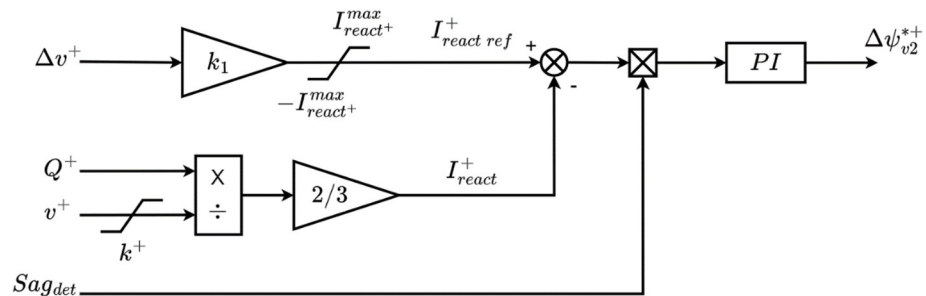


Figure 8. Positive reactive current controller block.

Therefore, in order to obtain the  $I_{react\ ref}^+$ , a  $K_1$  factor is applied to the positive sequence voltage error obtained and limiting its value to 1 and  $-1$  p.u. The values of  $K_1$  and  $K_2$  for negative sequence are fixed at a certain value but, in the event that the sum of  $I_{react\ ref}^+$  and  $I_{react\ ref}^-$  exceeds 1 p.u., their value is automatically readjusted to ensure that it always satisfies that:

$$K_{1,2} * (\Delta v^+ + \Delta v^-) \leq 1 \tag{19}$$

Then, when a voltage dip is detected, the error between  $I_{react\ ref}^+$  and the positive sequence reactive current module  $I_{react}^+$  is passed through a PI regulator to obtain  $\Delta\psi_{v2}^{*+}$ , which modifies the module of the positive sequence virtual-flux reference until the  $I_{react\ ref}^+$  is reached. The  $I_{react}^+$  current is calculated from:

$$Q^+ = \frac{3}{2} v^+ I_{react}^+ \tag{20}$$

where the positive sequence module of the voltage  $v^+$  is also limited to a value greater than zero ( $k^+$ ) to avoid indeterminacies.

Therefore, the module of the positive sequence virtual-flux reference  $\psi_v^{*+}$  is obtained as follows:

$$\psi_v^{*+} = \psi_{v0}^+ + n_q(Q^+ - Q^{*+}) + \Delta\psi_{v1}^{*+} + \Delta\psi_{v2}^{*+} \tag{21}$$

In Table A1 of Appendix A, it can be seen that the PI controller gains for the ACC+ and RCC+ blocks are different. This is due to the fact that the ACC+ controller acts directly on the control angle, which can worsen the system response in case of oscillations. In contrast, the RCC+ controller acts directly on the magnitude of the virtual flux, enabling a faster response without compromising the system behavior.

Lastly, the control scheme of the virtual-flux orientation (VFOC) depicted in Figure 4 is shown in Figure 9, which calculates the positive sequence converter voltage references  $e_d^+$  and  $e_q^+$ . In order to obtain the positive sequence dq components of the virtual flux, a Park transformation ( $\alpha\beta$ -dq) is applied to  $\psi_{\alpha v}^+$  and  $\psi_{\beta v}^+$ , calculated through the VFM block.

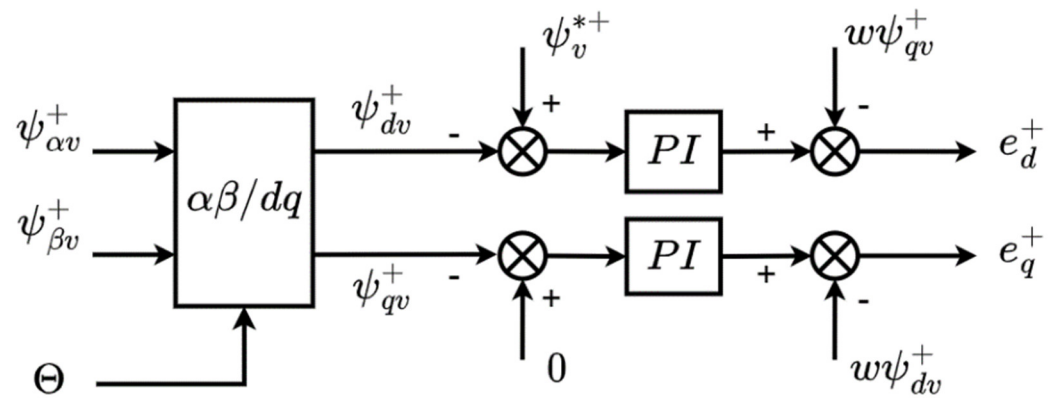


Figure 9. Virtual-flux orientation controller block.

After that, the q component  $\psi_{qv}^+$  is compared to 0 to align the virtual-flux module to the d-axis. Meanwhile, the d component  $\psi_{dv}^+$  is compared to the flux module reference  $\psi_v^{*+}$  calculated in the  $RPC^+$  loop. Both error signals are passed through two PI regulators and then feedforward signals are added to compensate the cross-coupling terms.

#### 4.3. Negative Sequence Control Scheme

To fulfill the current absorption/injection requirements during unbalanced faults of the Spanish grid code, the negative sequence control scheme shown in Figure 10 has been implemented. The proposed control is composed by three different blocks, obtaining as outputs the negative sequence converter voltage references  $e_d^-$  and  $e_q^-$ .

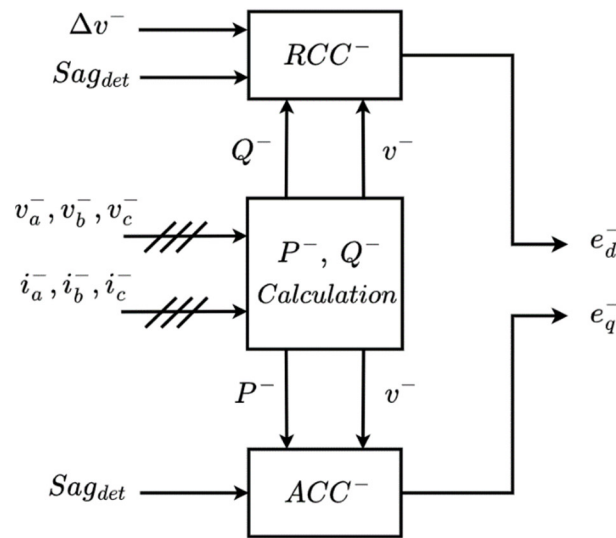


Figure 10. Negative sequence control scheme.

The  $P^-, Q^-$  calculation block obtains the negative sequence active and reactive powers in a similar way to (8) and (9) but using the negative sequence voltages and currents, resulting in:

$$P^- = \frac{3}{2} (v_{\alpha}^- i_{\alpha}^- + v_{\beta}^- i_{\beta}^-) \tag{22}$$

$$Q^- = \frac{3}{2} (v_{\beta}^- i_{\alpha}^- - v_{\alpha}^- i_{\beta}^-) \tag{23}$$

The negative reactive current controller ( $RCC^-$ ) block is shown in Figure 11 and operates in a very similar way as the  $RCC^+$  loop. As required by the Spanish grid code, when an unbalanced fault occurs, the converter must inject negative sequence reactive current additional to the pre-fault reactive current and proportional to the negative sequence voltage error ( $\Delta v^-$ ). As the pre-fault negative sequence reactive current is zero before the fault, the  $I_{react\ ref}^-$  is assumed equal to  $\Delta I_{react}^-$ .

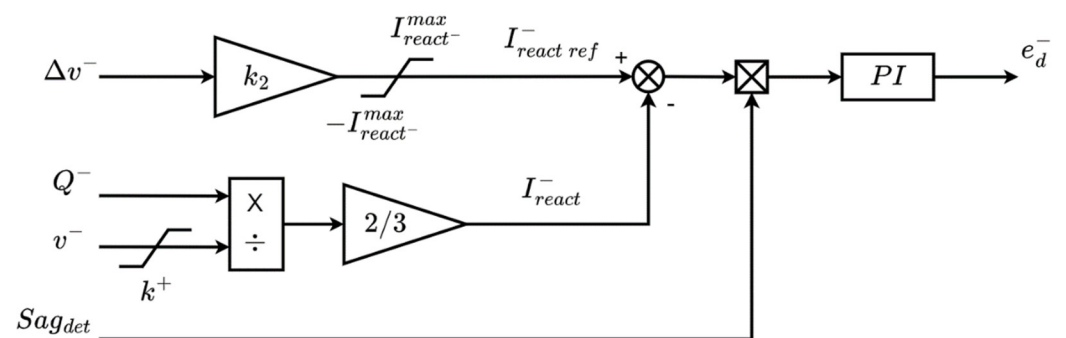


Figure 11. Negative reactive current controller block.

To obtain the  $I_{react\ ref}^-$ , a  $K_2$  factor is applied to the negative sequence voltage error measured. In addition, the reference value is limited to 1 and -1 p.u. As with  $K_1$ , its value is fixed at a certain value but is automatically readjusted when the sum of  $I_{react\ ref}^+$  and  $I_{react\ ref}^-$  exceeds 1 p.u. to ensure that the converter currents always satisfy (19).

Then, when a voltage dip is detected, the error between  $I_{react\ ref}^-$  and the negative sequence reactive current module  $I_{react}^-$  is passed through a regulator to obtain  $e_d^-$ . As a particular feature of this block, the PI gain must be of a negative sign because the modulus

of  $I_{react}^-$  and the current component  $i_d^-$  are of the opposite sign. The  $I_{react}^-$  current is calculated similarly to (19) from the following equation:

$$Q^- = \frac{3}{2} v^- I_{react}^- \tag{24}$$

where the negative sequence module of the voltage  $v^-$  is also limited to a value greater than zero ( $k^+$ ) to avoid indeterminacies.

The negative active current controller ( $ACC^-$ ) block depicted in Figure 10 is illustrated in Figure 12. This block operates as the  $ACC^+$  but, in this case, the reference is set to 0 in order to not inject negative sequence active current during the fault. As for the  $RCC^-$ , the gain of the PI regulator must be negative since the modulus of  $I_{act}^-$  and the negative sequence component  $i_q^-$  are opposite. The  $I_{act}^-$  current is calculated from:

$$P^- = \frac{3}{2} v^- I_{act}^- \tag{25}$$

where the positive sequence module of the voltage  $v^-$  is limited to a value greater than zero ( $k^+$ ) to avoid indeterminacies.

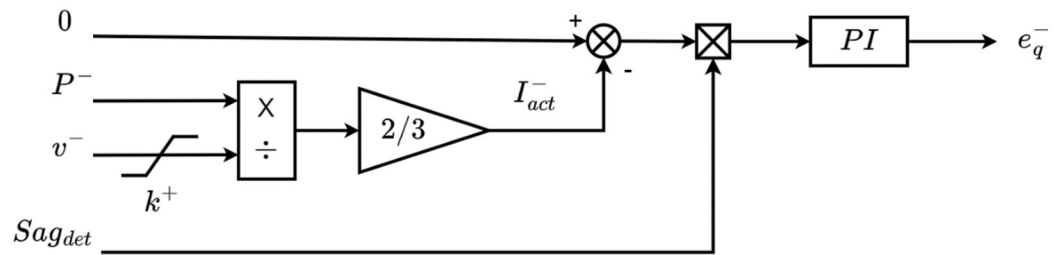


Figure 12. Negative active current controller block.

#### 4.4. Converter Voltage Setpoints Calculation

Once the converter voltage references of both sequences  $e_d^+$ ,  $e_q^+$ ,  $e_d^-$ , and  $e_q^-$  are obtained, the algorithm shown in Figure 13 is applied to calculate the phase voltages of the converter  $e_a, e_b, e_c$ . First, the Park transform is applied, using the control angle  $\theta$  for the positive sequence and  $\theta'$  for the negative sequence, being  $\theta' = -\theta$ . Then, the two components are added to obtain the three phase voltages of the converter.

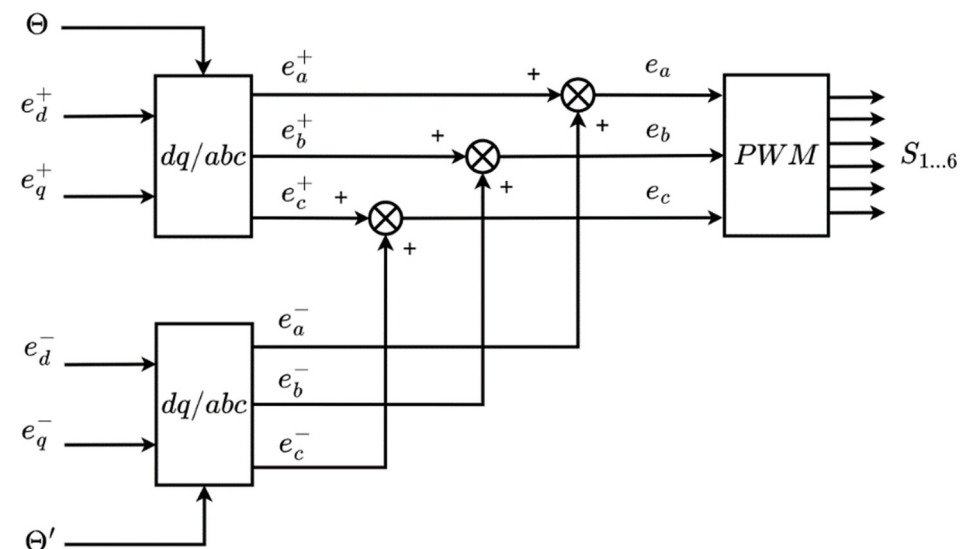


Figure 13. Converter voltage setpoints calculation.

Finally, the switching pattern of the converter  $S_{1...6}$  is generated using a pulse width modulation (PWM) algorithm.

## 5. Real-Time HIL Simulation Results

This section presents the results obtained using the proposed control scheme under balanced and unbalanced faults at point F in Figure 1 and compared to the response of the original control strategy. All the results presented were obtained using the hardware in the loop experimental set-up shown in Figure 14, which includes the real-time digital simulator (RTDS), where the plant shown in Figure 1 has been modeled in RSCAD and the real-time controller (dSPACE). The parameters used to configure the model in RSCAD and the control system are given in Table A1 of Appendix A and Table A2 of Appendix B, respectively. Finally, it should be noted that the requirements set by the Spanish grid code refer to the rms value of the voltage and current, while, in the graphs shown in this section, what is read is their peak value.



**Figure 14.** Hardware in the loop experimental set-up.

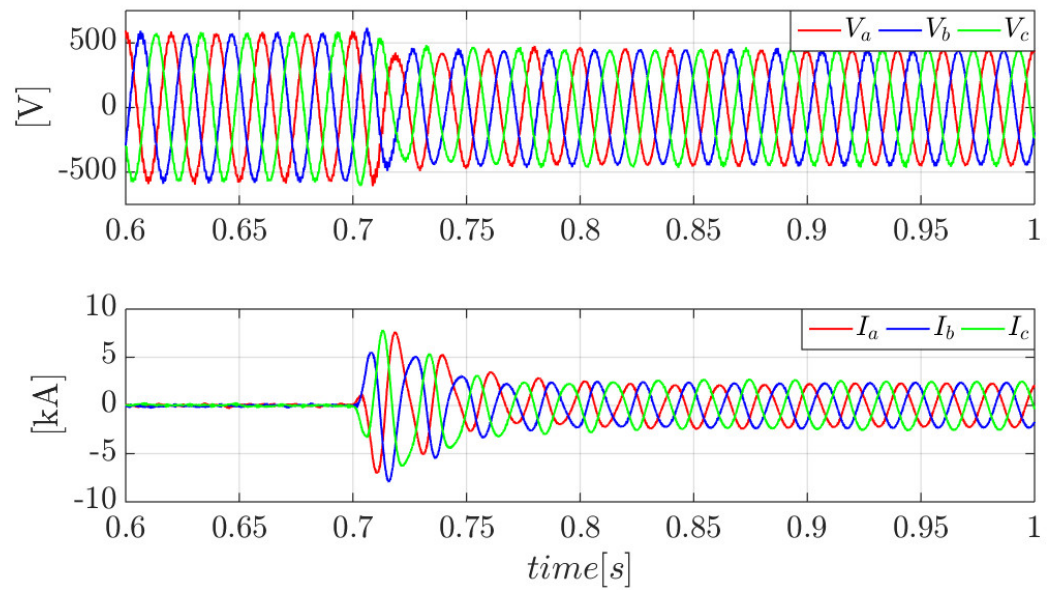
### 5.1. Balanced Three-Phase Faults

Figure 15 shows the instantaneous currents and voltages at the converter output during a balanced three-phase fault simulated at point F in Figure 1. At time  $t = 0.7$  s, the voltage drops to 0.78 p.u. From there, the converter starts to inject positive sequence reactive current proportional to the voltage error.

For this test, a value of  $K_1$  equal to 2 was set, so the amount of reactive current injected, as shown in Figure 16, is 0.44 p.u. In addition, sufficient active current is injected during the fault to reach the nominal value of the converter's current.

In order to verify the robustness of the proposed control system under balanced faults, the same test has been performed again but with a depth of approximately 0.95 p.u. Figure 17 shows the instantaneous currents and voltages at the converter output during the fault, with similar behavior to the previous case.

Figure 18 shows how the converter only injects positive sequence reactive current during the voltage dip, reaching its nominal value (1 p.u.). With a value of  $K_1$  equal to 2, for a voltage drop of 0.95 p.u., the converter should provide 1.9 p.u. but the limiter shown in Figure 8 does not allow the reference to be greater than 1 p.u. in these cases.



**Figure 15.** GFM converter instantaneous voltage and currents during a balanced fault with 0.22 p.u. depth.

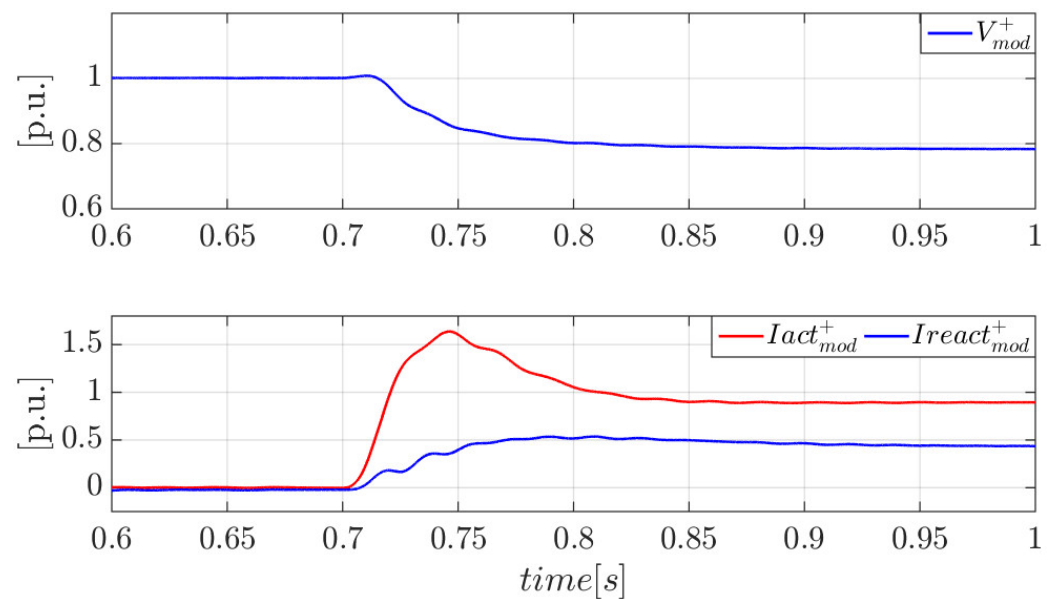


**Figure 16.** GFM converter positive sequence voltage and currents during a balanced fault with 0.22 p.u. depth.

Finally, Table 2 shows a summary of the results obtained during this section.

**Table 2.** Summary of the results obtained under balanced faults.

Cases	$I_{act}^+$	$I_{react}^+$	$K_1$ and $K_2$ Set Value	$K_1$ and $K_2$ Real Value
$\Delta v^+ = 0.22$ p.u.	0.9 p.u.	0.44 p.u.	2	2
$\Delta v^+ = 0.95$ p.u.	0 p.u.	1 p.u.	2	1.05

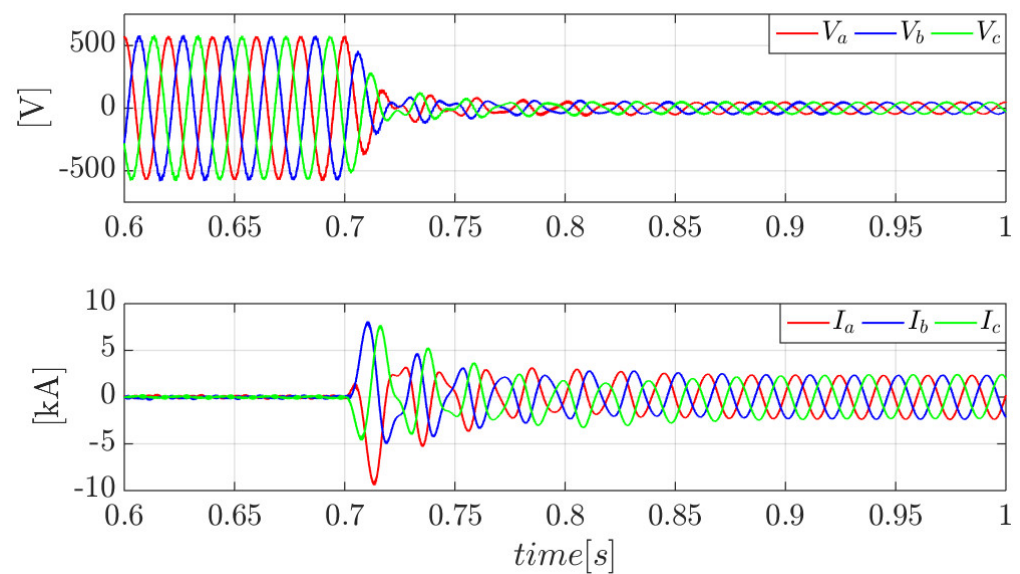


**Figure 17.** GFM converter instantaneous voltage and currents during a balanced fault with 0.95 p.u. depth.

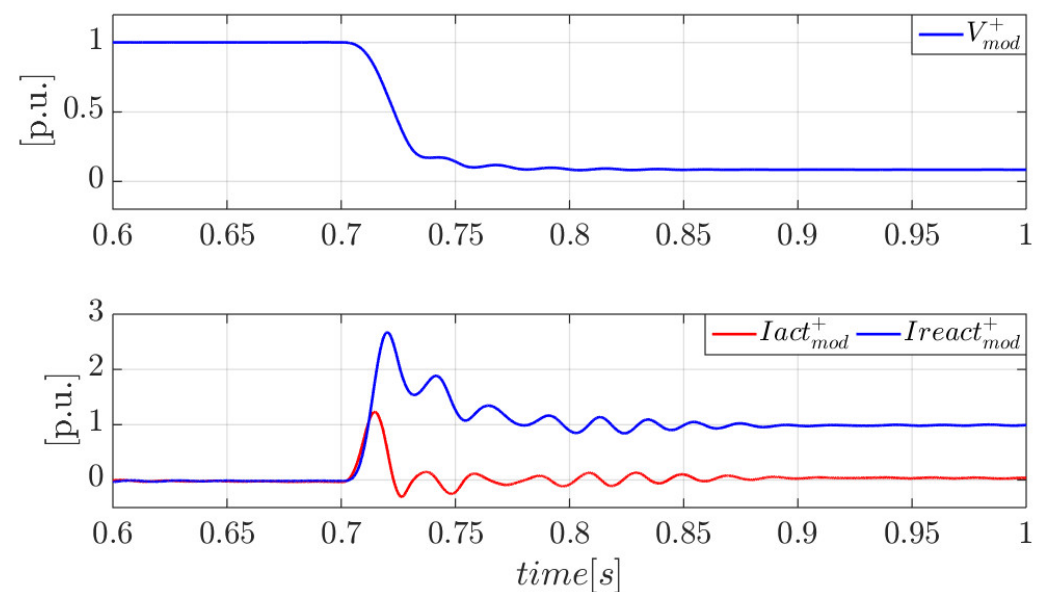
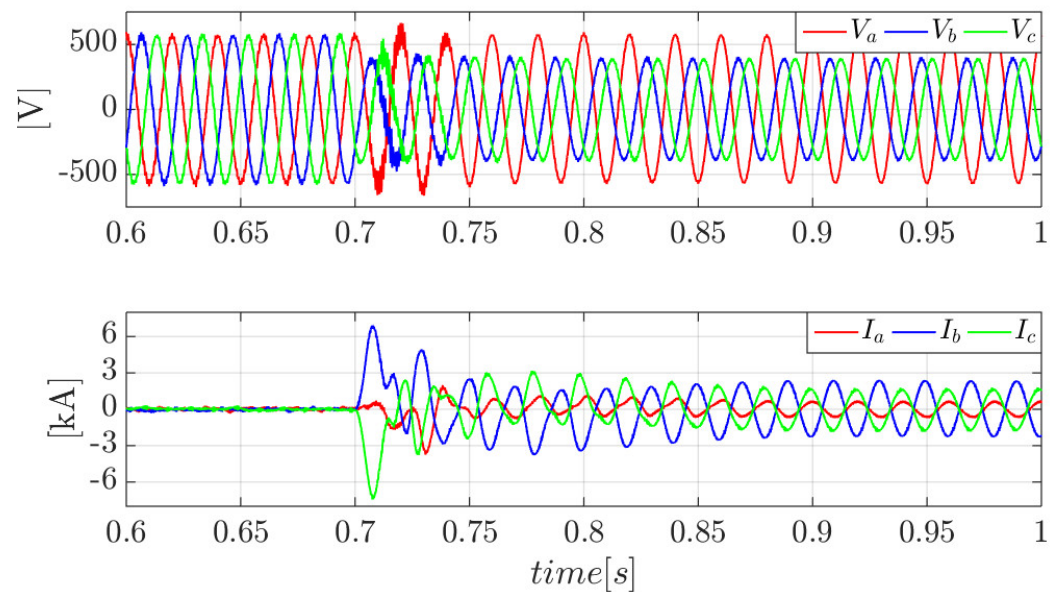


**Figure 18.** GFM converter positive sequence voltage and currents during a balanced fault with 0.95 p.u. depth.

### 5.2. Unbalanced Phase-to-Phase Faults

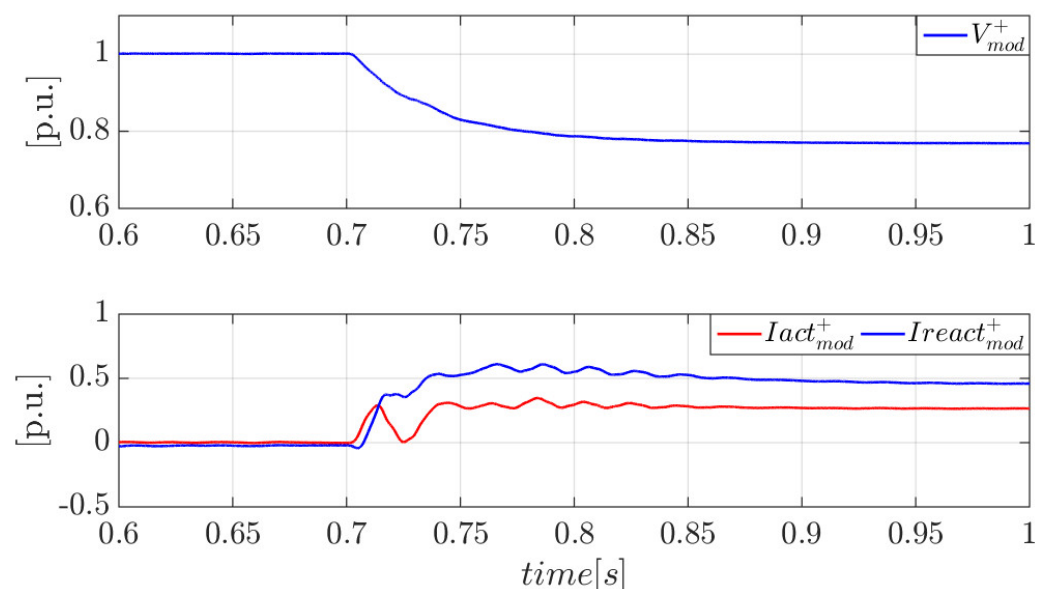
To test the negative sequence response of the virtual-flux-based GFM converter with the proposed sequence control scheme, an unbalanced phase-to-phase fault has been simulated at point F in Figure 1. Figure 19 shows the instantaneous voltages and currents during the fault.

At time  $t = 0.7$  s, the fault occurs, leading to a voltage and current unbalance. After the transient, the converter's output voltage decreases to 0.77 p.u., while the current, as requested by the Spanish grid code, reaches the nominal value (1 p.u.).



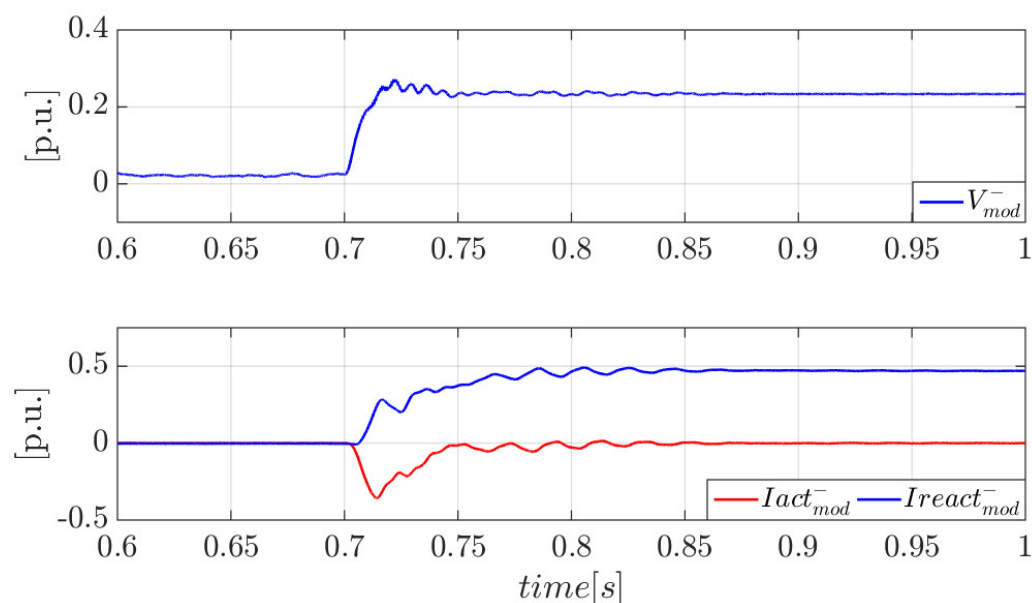
**Figure 19.** GFM converter instantaneous voltage and currents during an unbalanced fault with 0.23 p.u. depth.

Figure 20 shows the modules of voltage, active current, and reactive current of positive sequence during the fault. As the voltage drops 0.23 p.u., the positive sequence reactive current to be injected is that difference multiplied by the constant  $K_1$ , equal to 2 for this test. Therefore, and as can be observed in the graph below, the positive reactive current generated by the converter is 0.46 p.u. The positive sequence active current supplied is that necessary to reach the total converter's current nominal value.



**Figure 20.** GFM converter positive sequence voltage and currents during an unbalanced fault with 0.23 p.u. depth.

Finally, Figure 21 shows the converter negative sequence voltage and currents during the fault. As established by the Spanish grid code, during the unbalanced fault, the converter must provide a negative sequence reactive current proportional to the negative sequence voltage error ( $\Delta v^-$ ).



**Figure 21.** GFM converter negative sequence voltage and currents during an unbalanced fault with 0.23 p.u. depth.

As for the positive sequence, the voltage error is approximately 0.23 p.u. and the negative sequence reactive current provided by the converter for a  $K_2$  equal to 2 is 0.46 p.u. In addition, the negative sequence active current is set to 0 during the fault.

As in the previous section, the test has been repeated but simulating a phase-to-phase fault with a depth of 0.5 p.u., which means that the voltage between two of the phases is practically zero. Figure 22 shows the instantaneous voltages and currents during the fault.

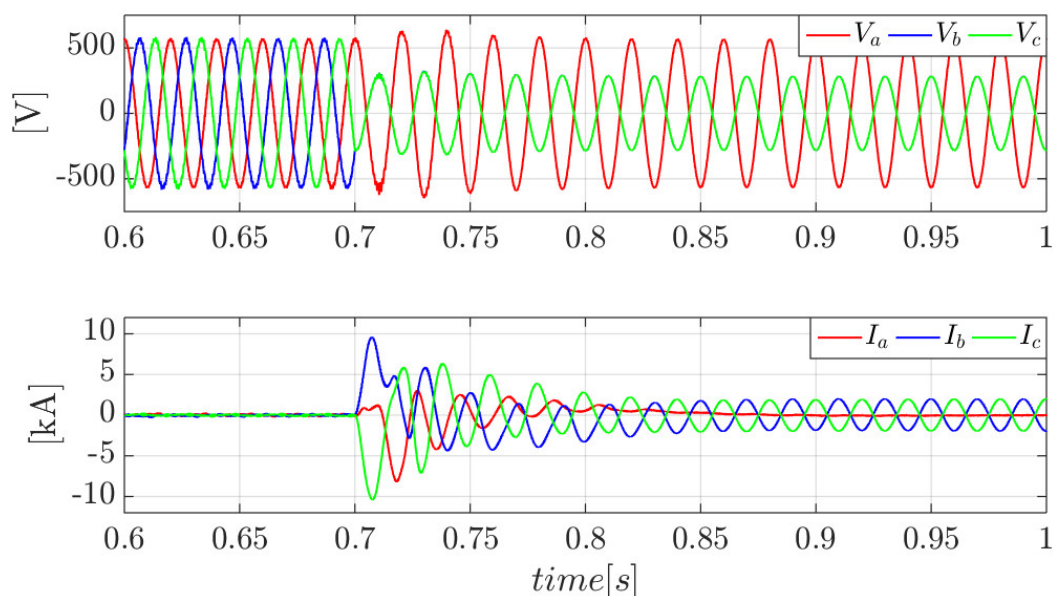


**Figure 22.** GFM converter instantaneous voltage and currents during an unbalanced fault with 0.5 p.u. depth.

In the event of a fault with a depth of 0.5 p.u., the converter would inject 1 p.u. of positive sequence reactive current and 1 p.u. of negative sequence reactive current. As this would result in exceeding the maximum current allowed by the converter, the constants

$K_1$  and  $K_2$  are recalculated to ensure that the converter output current reaches its rated value.

Figures 23 and 24 show positive and negative sequence voltages and currents during the fault. Compared to the previous case, the maximum possible reactive current is being provided, having already reached the rated value and, therefore, the converter does not need to inject positive sequence active current.

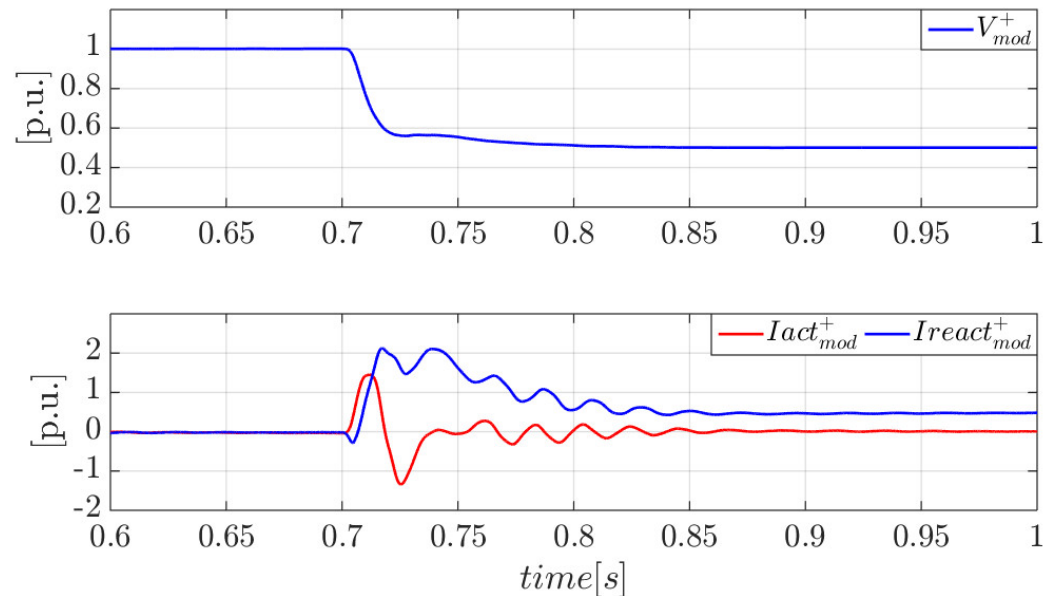


**Figure 23.** GFM converter positive sequence voltage and currents during an unbalanced fault with 0.5 p.u. depth.

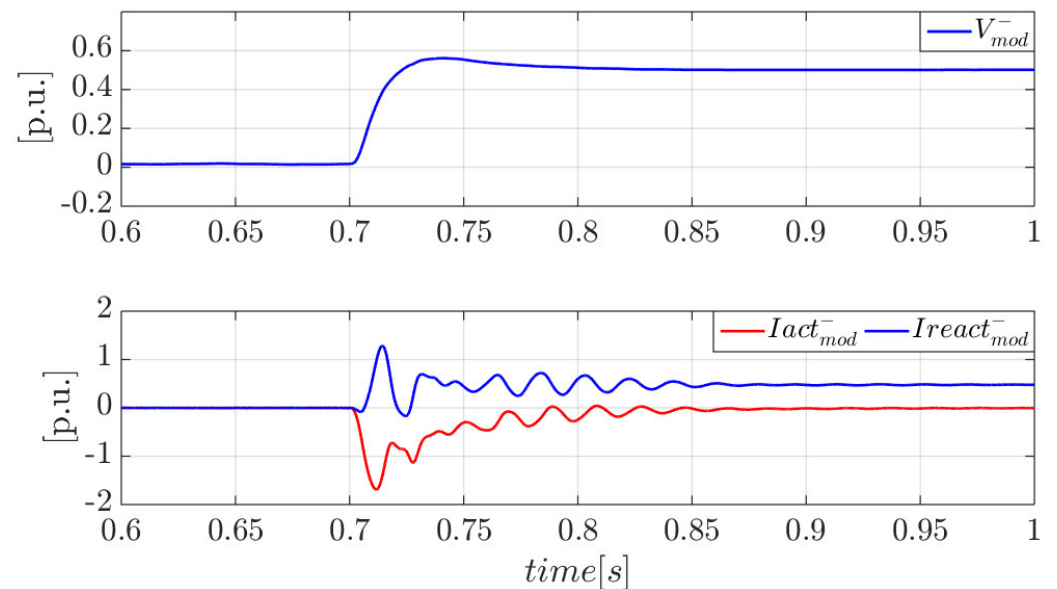


**Figure 24.** GFM converter negative sequence voltage and currents during an unbalanced fault with 0.5 p.u. depth.

Table 3 shows a summary of the results obtained during this section.

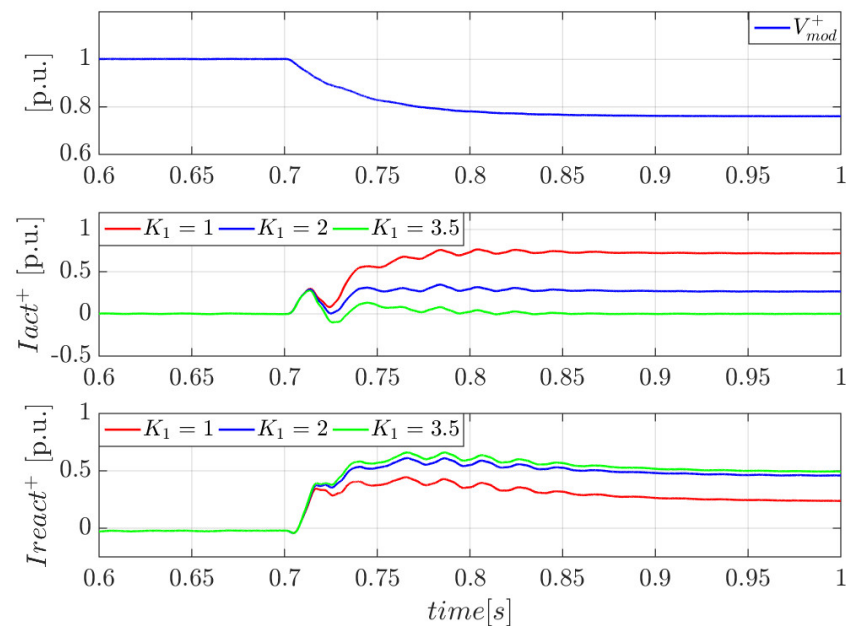
**Table 3.** Summary of the results obtained under unbalanced faults.

Cases	$I_{act}^+$	$I_{react}^+$	$I_{act}^-$	$I_{react}^-$	$K_1$ and $K_2$ Set Value	$K_1$ and $K_2$ Real Value
$\Delta v^- = 0.23$ p.u.	0.28 p.u.	0.46 p.u.	0 p.u.	0.46 p.u.	2	2
$\Delta v^- = 0.5$ p.u.	0 p.u.	0.5 p.u.	0 p.u.	0.5 p.u.	2	1

### 5.3. Converter Response to Unbalanced Phase-to-Phase Faults for Different Values of $K_1$ and $K_2$

The values of  $K_1$  and  $K_2$  are configurable within the range  $2 \leq K_{1,2} \leq 6$ . For this test, the same unbalanced fault at point F in Figure 1 has been simulated as in the previous section but modifying the value of  $K_1$  and  $K_2$ . The values chosen for this test have been  $K_1 = K_2 = 3.5$ ,  $K_1 = K_2 = 2$ , and  $K_1 = K_2 = 1$ . The decision to test the last value of  $K_1$  and  $K_2$  even though it is out of the range set by the Spanish grid code has been made to see how the model is able to provide more positive sequence active current when reactive current references are lower.

The modules of the positive sequence voltage, active current, and reactive current during the fault for the different values of  $K_1$  are shown in Figure 25. For the same positive sequence voltage error, the reactive current injected increases as the value of  $K_1$  is higher and, as a consequence, the active current provided by the converter to reach the rated current decreases.

**Figure 25.** GFM converter positive sequence voltage and currents during the unbalanced fault for  $K_1$  and  $K_2$  different values.

When  $K_1 = 3.5$ , the amount of positive and negative sequence reactive current that should be provided by the converter for a voltage error of 0.23 p.u. exceeds the total current limit allowed by the VSC. Therefore, for these cases, although the constants are set to 3.5, they actually have another value, which in this particular case is 2.17. In addition, as the maximum current value is reached only with the reactive current provided by the converter, no positive sequence active current is injected during the fault.

Finally, Figure 26 shows how, for the negative sequence, something similar to the positive sequence occurs. The higher the value of  $K_2$ , the higher the current supplied by the converter. When  $K_2 = 3.5$ , the model modifies the  $K_2$  real value in order to not exceed the total current limit allowed by the VSC.

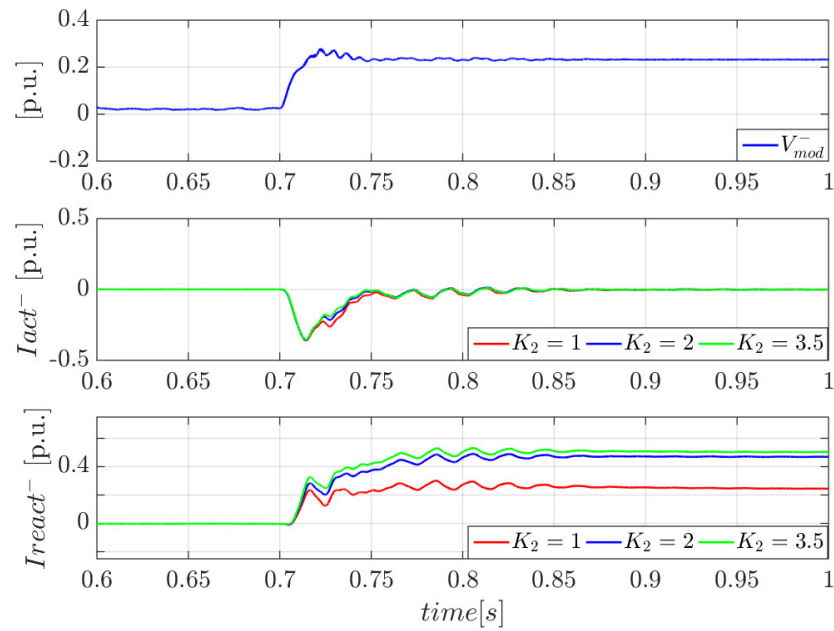


**Figure 26.** GFM converter negative sequence voltage and currents during the unbalanced fault for  $K_1$  and  $K_2$  different values.

Table 4 shows a summary of the results obtained during this section.

**Table 4.** Summary of the results obtained for different values of  $K_1$  and  $K_2$ .

$K_1$ and $K_2$ Set Value	$I_{act}^+$	$I_{react}^+$	$I_{act}^-$	$I_{react}^-$	$K_1$ and $K_2$ Real Value
$K_1 = K_2 = 1$	0.72 p. u.	0.24 p. u.	0 p. u.	0.24 p. u.	1
$K_1 = K_2 = 2$	0.28 p. u.	0.46 p. u.	0 p. u.	0.46 p. u.	2
$K_1 = K_2 = 3.5$	0 p. u.	0.5 p. u.	0 p. u.	0.5 p. u.	2.17

#### 5.4. Comparison between the Original and the Proposed Model

To compare the proposed model with the original one, the same unbalanced fault as in the previous sections has been simulated. Figure 27 shows the positive sequence voltage and currents modulus of both models during the voltage dip. The original model does not provide active current, while the proposed model does in order to achieve the rated current value of the converter. On the other hand, the original model provides a higher amount of reactive current than the proposed model with  $K_1 = 2$ .

Finally, the negative sequence currents and voltage modulus are shown in Figure 28 for a  $K_2$  equal to 2. During the fault, the negative sequence active current injected by both models is practically 0. On the other hand, the reactive current provided by the VSC in the proposed model is proportional to the negative sequence voltage error. However, in the original model, the maximum current allowed in the VSC is exceeded. This is because the current limiters of the original control strategy only operate over the positive sequence currents.

Table 5 shows a summary of the results obtained during this section.

**Table 5.** Summary of the results obtained during the comparison.

	$I_{act}^+$	$I_{react}^+$	$I_{act}^-$	$I_{react}^-$
Original Model	0 p. u.	0.75 p. u.	-0.02 p. u.	1.28 p. u.
Proposed Model	0.28 p. u.	0.46 p. u.	0 p. u.	0.46 p. u.

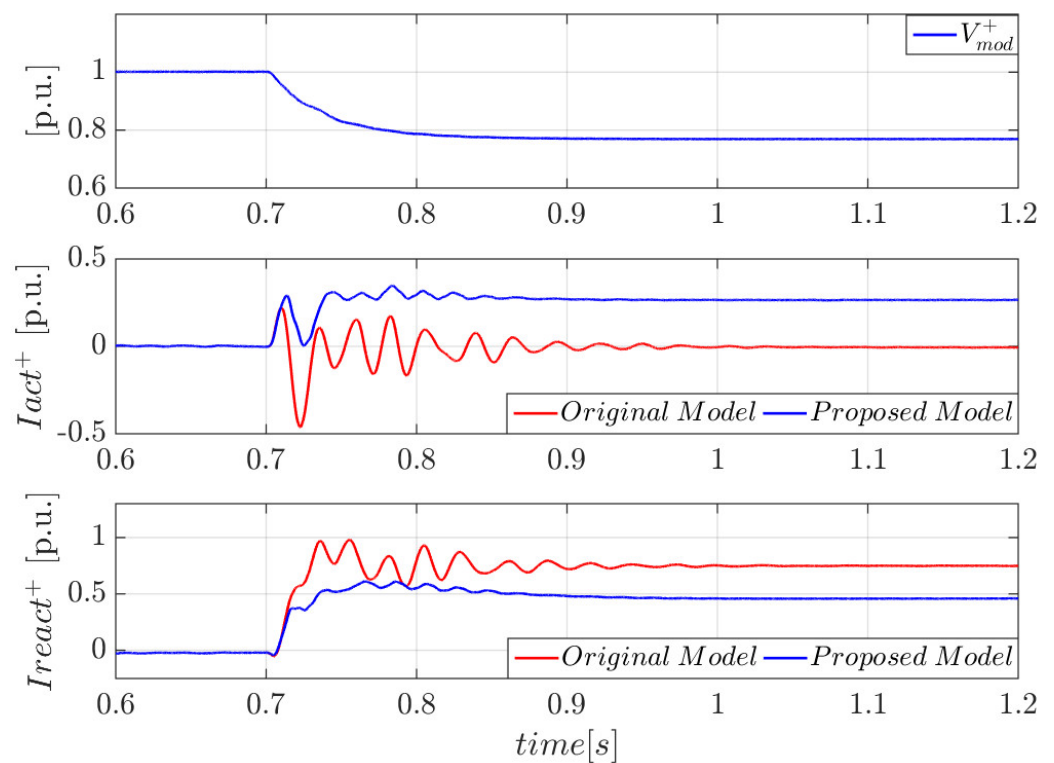


**Figure 27.** Positive sequence voltage and currents during the unbalanced fault for both models.

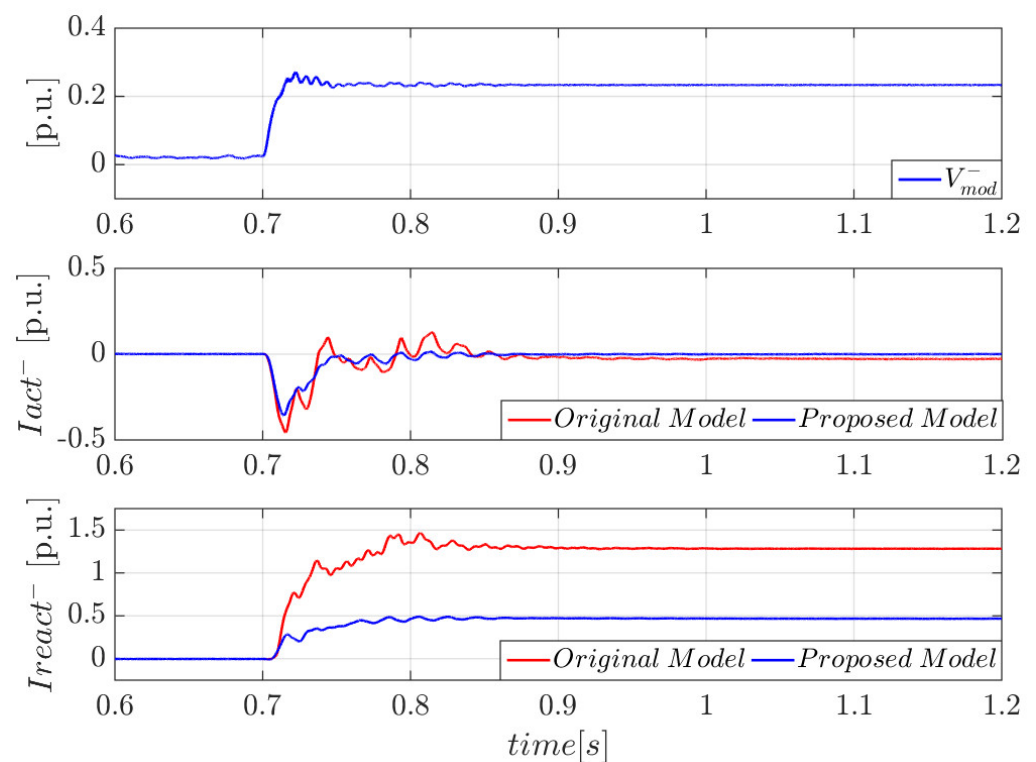


**Figure 28.** Negative sequence voltage and currents during the unbalanced fault for both models.

## 6. Conclusions

A novel strategy for controlling the sequence component of a GFM converter based on the virtual flux during unbalanced faults has been proposed. The main conclusion based on the results obtained is that the proposed GFM sequence control scheme based

on virtual flux satisfies the Spanish grid code requirements for converters during balanced and unbalanced faults.

During balanced faults, the converter is able to provide a positive sequence reactive current proportional to the voltage drop, which depends on the setting of a proportional constant  $K_1$ . In addition, for unbalanced faults, the converter also provides negative sequence reactive current proportional to the negative sequence voltage error. The amount of negative sequence reactive current depends on the value set for  $K_2$ . If the positive plus negative sequence reactive currents to be supplied by the VSC based on the set  $K_1$  and  $K_2$  values exceed the maximum current allowed by the converter, the maximum reactive current supplied by the converter is set to 1 p.u., modifying the real value of the  $K_1$  and  $K_2$  constants in order to protect the VSC.

On the other hand, for both types of faults, the converter injects positive sequence active current until the rated value of the total current is reached at the converter output if there is remaining current headroom.

Finally, a comparison has been made between the proposed control system and the original control strategy based on the virtual-flux orientation, where it is shown how under unbalanced faults the original model is not able to control and limit the negative sequence currents. The future perspective of this work is that virtual-flux-based GFM can be used and commercialized to support the increasing use of renewable energy sources, which means testing industrial prototypes as a first step in future works.

**Author Contributions:** Conceptualization, J.L.R.-A., S.A. and J.E.-G.; Methodology, J.L.R.-A., S.A., J.E.-G. and J.D.F.; Software, J.D.F.; Validation, J.L.R.-A., S.A., J.E.-G. and J.D.F.; Investigation, J.L.R.-A., S.A., J.E.-G. and J.D.F.; Data curation, J.L.R.-A., S.A. and J.E.-G.; Writing—original draft preparation, J.D.F.; Writing—review and editing, J.L.R.-A., S.A. and J.E.-G.; Visualization, J.D.F.; Supervision, J.L.R.-A., S.A. and J.E.-G. All authors have read and agreed to the published version of the manuscript.

**Funding:** This paper was supported by the Spanish Research Agency under project reference PID2019-106028RB-I00/AEI/10.13039/501100011033.

**Data Availability Statement:** Not applicable.

**Conflicts of Interest:** The authors declare no conflict of interest.

## Appendix A. RSCAD Parameters

Table A1 shows all the parameters used to configure the system in RSCAD.

**Table A1.** System parameters.

Parameters	Value	Units
DC voltage of the VSC, $V_{dc}$	1200	V
Converter rated power, $S_n$	2	MVA
Line to line rated voltage (RMS), $V_n$	690	V
Filter inductance, $L_f$	0.113	mH
Filter resistance, $R_f$	0.714	m $\Omega$
Filter capacitance, $C_f$	0.5	mF
Nominal frequency, $f_n$	50	Hz
Switching frequency, $f_{sw}$	3	kHz
Grid inductance, $L_g$	56.5	$\mu$ H
Grid resistance, $R_g$	0.357	$\mu\Omega$
Short-circuit ratio, SCR	2	
X/R ratio	10	
$T_t$ : power rating, $S_N$	2	MVA
$T_t$ : rated line–line voltage primary, $V_{1N}$	20	kV

$T_t$ : rated line–line voltage secondary, $V_{2N}$	0.69	kV
$T_t$ : frequency	50	Hz

## Appendix B. Control System Parameters

The values used in the control system are shown in Table A2.

**Table A2** Control system parameters.

Parameters	Value	Units
Inertia, $T_m$	15	s
Damping constant, $D$	50	p.u.
PSS time constant, $T_w$	1.2	s
PSS constant, $K_w$	0.01	
PI Gain, $ACC^+$	0.12	
PI Time constant, $ACC^+$	0.01	s
PI Gain, $RCC^+$	0.3	
PI Time constant, $RCC^+$	0.04	s
PI Gain, $ACC^-$	−0.5	
PI Time constant, $ACC^-$	0.085	s
PI Gain, $RCC^-$	−0.5	
PI Time constant, $RCC^-$	0.085	s
PI Gain, $VFOC$	1	
PI Time constant, $VFOC$	0.16	s

## References

- Christensen, P.; Andersen, G.K.; Seidel, M.; Bolik, S.; Engelken, S.; Knueppel, T.; Krontiris, A.; Wuerflinger, K.; Bülo, T.; Jahn, J.; et al. *High Penetration of Power Electronic Interfaced Power Sources and the Potential Contribution of Grid Forming Converters*; ENTSO-E 2020; ENTSO: Brussels, Belgium, 2020.
- International Renewable Energy Agency (IRENA). *Renewable Energy Statistics 2021*; IRENA: Abu Dhabi, United Arab Emirates, 2021; ISBN 978-92-9260-356-4.
- Matevosyan, J.; Vital, V.; O’Sullivan, J.; Quint, R.; Badrzadeh, B.; Prevost, T.; Quitmann, E.; Ramasubramanian, D.; Urdal, H.; Achilles, S.; et al. Grid-Forming Inverters: Are They the Key for High Renewable Penetration? *IEEE Power Energy Mag.* **2019**, *17*, 89–98. <https://doi.org/10.1109/mpe.2019.2933072>.
- Rathnayake, D.B.; Akrami, M.; Phurailatpam, C.; Me, S.P.; Hadavi, S.; Jayasinghe, G.; Zabihi, S.; Bahrani, B. Grid Forming Inverter Modeling, Control, and Applications. *IEEE Access* **2021**, *9*, 114781–114807. <https://doi.org/10.1109/access.2021.3104617>.
- Matevosyan, J.; MacDowell, J.; Miller, N.; Badrzadeh, B.; Ramasubramanian, D.; Isaacs, A.; Quint, R.; Quitmann, E.; Pfeiffer, R.; Urdal, H.; et al. A Future With Inverter-Based Resources: Finding Strength From Traditional Weakness. *IEEE Power Energy Mag.* **2021**, *19*, 18–28.
- Tielens, P.; Van Hertem, D. The relevance of inertia in power systems. *Renew. Sustain. Energy Rev.* **2016**, *55*, 999–1009.
- Rosso, R.; Wang, X.; Liserre, M.; Lu, X.; Engelken, S. Grid-Forming Converters: Control Approaches, Grid-Synchronization, and Future Trends—A Review. *IEEE Open J. Ind. Appl.* **2021**, *2*, 93–109. <https://doi.org/10.1109/ojia.2021.3074028>.
- Zhang, H.; Xiang, W.; Lin, W.; Wen, J. Grid Forming Converters in Renewable Energy Sources Dominated Power Grid: Control Strategy, Stability, Application, and Challenges. *J. Mod. Power Syst. Clean Energy* **2021**, *9*, 1239–1256. <https://doi.org/10.35833/mpce.2021.000257>.
- Chandorkar, M.; Divan, D.; Adapa, R. Control of parallel connected inverters in stand-alone AC supply systems. *IEEE Trans. Ind. Appl.* **1993**, *29*, 136–143. <https://doi.org/10.1109/ias.1991.178359>.
- Hart, P.; Lesieutre, B. Energy function for a grid-tied, droop-controlled inverter. In Proceedings of the 2014 North American Power Symposium (NAPS), Pullman, WA, USA, 7–9 September 2014.
- D’Arco, S.; Suul, J.A. Equivalence of Virtual Synchronous Machines and Frequency-Droops for Converter-Based MicroGrids. *IEEE Trans. Smart Grid* **2013**, *5*, 394–395. <https://doi.org/10.1109/tsg.2013.2288000>.
- Beck, H.-P.; Hesse, R. Virtual synchronous machine. In Proceedings of the 2007 9th International Conference on Electrical Power Quality and Utilisation, Barcelona, Spain, 9–11 October 2007; pp. 1–6.
- Driesen, J.; Visscher, K. Virtual synchronous generators. In Proceedings of the 2008 IEEE Power and Energy Society General Meeting—Conversion and Delivery of Electrical Energy in the 21st Century, Pittsburgh, PA, USA, 20–24 July 2008.

14. Liu, J.; Miura, Y.; Bevrani, H.; Ise, T. Enhanced Virtual Synchronous Generator Control for Parallel Inverters in Microgrids. *IEEE Trans. Smart Grid* **2017**, *8*, 2268–2277. <https://doi.org/10.1109/tsg.2016.2521405>.
15. Zhong, Q.-C.; Nguyen, P.-L.; Ma, Z.; Sheng, W. Self-Synchronized Synchronverters: Inverters Without a Dedicated Synchronization Unit. *IEEE Trans. Power Electron.* **2014**, *29*, 617–630. <https://doi.org/10.1109/tpel.2013.2258684>.
16. Johnson, B.B.; Dhople, S.V.; Hamadeh, A.O.; Krein, P.T. Synchronization of Parallel Single-Phase Inverters with Virtual Oscillator Control. *IEEE Trans. Power Electron.* **2014**, *29*, 6124–6138. <https://doi.org/10.1109/tpel.2013.2296292>.
17. Johnson, B.B.; Dhople, S.V.; Cale, J.L.; Hamadeh, A.O.; Krein, P.T. Oscillator-Based Inverter Control for Islanded Three-Phase Microgrids. *IEEE J. Photovoltaics* **2014**, *4*, 387–395. <https://doi.org/10.1109/jphotov.2013.2280953>.
18. Groÿ, D.; Colombino, M.; Brouillon, J.; Dörfler, F. The effect of transmission-line dynamics on grid-forming dispatchable virtual-oscillator control. *IEEE Trans. Control Netw. Syst.* **2019**, *6*, 1148–1160.
19. Zubiaga, M.; Cardozo, C.; Prevost, T.; Sanchez-Ruiz, A.; Olea, E.; Izurza, P.; Khan, S.H.; Arza, J. Enhanced TVI for Grid Forming VSC under Unbalanced Faults. *Energies* **2021**, *14*, 6168. <https://doi.org/10.3390/en14196168>.
20. Quispe, J.C.; Orduña, E. Transmission line protection challenges influenced by inverter-based resources: A review. *Prot. Control. Mod. Power Syst.* **2022**, *7*, 28. <https://doi.org/10.1186/s41601-022-00249-8>.
21. Paquette, A.D.; Divan, D.M. Virtual Impedance Current Limiting for Inverters in Microgrids with Synchronous Generators. *IEEE Trans. Ind. Appl.* **2014**, *51*, 1630–1638. <https://doi.org/10.1109/tia.2014.2345877>.
22. Zarei, S.F.; Mokhtari, H.; Ghasemi, M.A.; Blaabjerg, F. Reinforcing Fault Ride Through Capability of Grid Forming Voltage Source Converters Using an Enhanced Voltage Control Scheme. *IEEE Trans. Power Deliv.* **2018**, *34*, 1827–1842. <https://doi.org/10.1109/tpwrd.2018.2844082>.
23. Bottrell, N.; Green, T.C. Comparison of Current-Limiting Strategies During Fault Ride-Through of Inverters to Prevent Latch-Up and Wind-Up. *IEEE Trans. Power Electron.* **2013**, *29*, 3786–3797. <https://doi.org/10.1109/tpel.2013.2279162>.
24. Fan, B.; Wang, X. Current-Limiting Control of Grid-Forming Inverters: State-of-the-Art and Open Issues. *TechRxiv* **2022**. <https://doi.org/10.36227/techrxiv.20430816.v1>.
25. Gkountaras, A.; Dieckerhoff, S.; Sezi, T. Evaluation of current limiting methods for grid forming inverters in medium voltage microgrids. In Proceedings of the 2015 IEEE Energy Conversion Congress and Exposition (ECCE), Montreal, QC, Canada, 20–24 September 2015; pp. 1223–1230.
26. Welck, F.; Duckwitz, D.; Gloeckler, C. Influence of virtual impedance on short circuit performance of virtual synchronous machines in the 9-bus system. In Proceedings of the NEIS 2017; Conference on Sustainable Energy Supply and Energy Storage Systems, Hamburg, Germany, 21–22 September 2017; VDE: Frankfurt am Main, Germany, 2017; pp. 1–7.
27. Glöckler, C.; Duckwitz, D.; Welck, F. Virtual synchronous machine control with virtual resistor for enhanced short circuit capability. In Proceedings of the 2017 IEEE PES Innovative Smart Grid Technologies Conference Europe (ISGT-Europe), Turin, Italy, 26–29 September 2017; pp. 1–6.
28. Camacho, A.; Castilla, M.; Miret, J.; Guzman, R.; Borrell, A. Reactive Power Control for Distributed Generation Power Plants to Comply with Voltage Limits During Grid Faults. *IEEE Trans. Power Electron.* **2014**, *29*, 6224–6234. <https://doi.org/10.1109/tpel.2014.2301463>.
29. Karimi, H.; Haddadi, A.; Karimi-Ghartemani, M.; Sadabadi, M. A Robust Vector Current Controller with Negative-Sequence Current Capability for Grid-Connected Inverters. *Energies* **2021**, *14*, 4549. <https://doi.org/10.3390/en14154549>.
30. Khan, A.; Ahmad, H.; Ahsan, S.M.; Gulzar, M.M.; Murawwat, S. Coordinated LVRT Support for a PMSG-Based Wind Energy Conversion System Integrated into a Weak AC-Grid. *Energies* **2021**, *14*, 6588. <https://doi.org/10.3390/en14206588>.
31. Baeckeland, N.; Herteleer, B.; Kleemann, M. Modelling fault behaviour of power electronic converters. *Int. J. Electr. Power Energy Syst.* **2020**, *123*, 106230. <https://doi.org/10.1016/j.ijepes.2020.106230>.
32. Jia, J.; Yang, G.; Nielsen, A.H. A Review on Grid-Connected Converter Control for Short-Circuit Power Provision Under Grid Unbalanced Faults. *IEEE Trans. Power Deliv.* **2018**, *33*, 649–661. <https://doi.org/10.1109/tpwrd.2017.2682164>.
33. Haddadi, A.; Farantatos, E.; Kocar, I.; Karaagac, U. Impact of Inverter Based Resources on System Protection. *Energies* **2021**, *14*, 1050. <https://doi.org/10.3390/en14041050>.
34. Haddadi, A.; Kocar, I.; Farantatos, E. *Impact of Inverter-Based Resources on Protection Schemes Based on Negative Sequence Components*; EPRI: Palo Alto, CA, USA, 2019.
35. Villén, M.T.; Comech, M.P.; Carrasco, E.M.; Hurtado, A.A.P. Influence of Negative Sequence Injection Strategies on Faulted Phase Selector Performance. *Energies* **2022**, *15*, 6018. <https://doi.org/10.3390/en15166018>.
36. VDE\_AR\_N\_4110 Technical Requirements for the Connection and Operation of Customer Installations to the Medium Voltage Network (TAR Medium Voltage). November 2018. Available online: <https://www.vde.com/en/fnn/topics/technical-connection-rules/tcr-for-medium-voltage> (accessed on 17 March 2023).
37. IPTO. Integration of the Regulation EU 631/2016 into the Greek Regulatory Framework, (Public Consultation Document). Available online: [https://www.admie.gr/sites/default/files/diaboyleyseis/attached-files2020/09/Integration\\_of\\_the\\_Regulation\\_EU\\_631-2016\\_into\\_the\\_Greek\\_Regulatory\\_Framework.pdf](https://www.admie.gr/sites/default/files/diaboyleyseis/attached-files2020/09/Integration_of_the_Regulation_EU_631-2016_into_the_Greek_Regulatory_Framework.pdf) (accessed on 17 March 2023).
38. Ministerio para la Transición Ecológica y el Reto Demográfico. Orden TED/749/2020, de 16 de Julio, Por La Que Se Establecen Los Requisitos Técnicos Para La Conexión a La Red Necesarios Para La Implementación de Los Códigos de Red de Conexión. 2020. BOE-A-2020-8965. pp. 62406–62458. Available online: <https://www.boe.es/eli/es/o/2020/07/16/ted749/con> (accessed on 7 July 2022).

39. Abubakar, M.; Renner, H.; Schürhuber, R. Development of a Novel Control Scheme for Grid-Following Converter under Asymmetrical Faults. *Energies* **2023**, *16*, 1276. <https://doi.org/10.3390/en16031276>.
40. Abubakar, M.; Akbari, H.; Renner, H. Development of Reference Current Calculation Scheme for Grid-Side Converter during Unbalanced Faults. In Proceedings of the 2022 2nd International Conference on Sustainable Mobility Applications, Renewables and Technology (SMART), Cassino, Italy, 23–25 November 2022; pp. 1–9.
41. Almeida, V.A.F.; Taranto, G.N.; Marinho, J.M.T. Phasor-domain Dynamic Model of Asymmetric Current Injection Controller for Converter-interfaced Generator. *J. Mod. Power Syst. Clean Energy* **2021**, *9*, 1269–1278. <https://doi.org/10.35833/mpce.2021.000407>.
42. Taul, M.G.; Wang, X.; Davari, P.; Blaabjerg, F. Current Reference Generation Based on Next-Generation Grid Code Requirements of Grid-Tied Converters During Asymmetrical Faults. *IEEE J. Emerg. Sel. Top. Power Electron.* **2020**, *8*, 3784–3797. <https://doi.org/10.1109/jestpe.2019.2931726>.
43. Rodríguez-Amenedo, J.L.; Gómez, S.A.; Zubiaga, M.; Izurza-Moreno, P.; Arza, J.; Fernández, J.D. Grid-Forming Control of Voltage Source Converters Based on the Virtual-Flux Orientation. *IEEE Access* **2023**, *11*, 10254–10274.

**Disclaimer/Publisher’s Note:** The statements, opinions and data contained in all publications are solely those of the individual author(s) and contributor(s) and not of MDPI and/or the editor(s). MDPI and/or the editor(s) disclaim responsibility for any injury to people or property resulting from any ideas, methods, instructions or products referred to in the content.